JOURNAL OF CATALYSIS 108, 452–466 (1987)

Ammonia Synthesis over a Supported Iron Catalyst Prepared from an Amorphous Iron-Zirconium Precursor

II. Surface Morphological Changes during the Genesis of the Catalyst

R. SCHLÖGL,* R. WIESENDANGER,† AND A. BAIKER‡

*Fritz-Haber Institut der Max Planck Gesellschaft, 1000 Berlin 33, Federal Republic of Germany; †Department of Physics, University of Basel, CH-4056 Basel, Switzerland; and ‡Department of Industrial and Engineering Chemistry, Swiss Federal Institut of Technology (ETH), ETH-Zentrum, CH-8092 Zürich, Switzerland

Received February 10, 1987; revised April 21, 1987

Amorphous $Fe_{91}Zr_9$, when exposed to ammonia synthesis conditions, undergoes drastic changes in the bulk and surface structure which finally lead to an active ammonia synthesis catalyst. Investigation of the surface morphology of the precursor using both scanning electron microscopy (SEM) and scanning tunneling microscopy (STM) revealed that the surface of the amorphous alloy is not flat, but consists of disk-shaped metal particles several hundred angstroms in size with clear valleys separating them. Upon activation, crystallization and reconstruction of the precursor surface occurs and results finally in the active catalyst consisting of iron particles stabilized by poorly crystalline zirconia. SEM showed that the active iron particles exist predominantly in the form of stacks of disks and well-developed crystals. Both morphologies are uncommon in conventional ammonia synthesis catalysts. The genesis of these morphologies is discussed based on the results of SEM and STM investigations.

INTRODUCTION

In the first part (*1*) of this series we reported on the development of the catalytic activity for ammonia synthesis of amorphous iron zirconium alloys during *in situ* activation. Tests of the catalytic activity and various analytical techniques showed that the amorphous precursor undergoes an irreversible transformation during activation under ammonia synthesis conditions. It is this transformation which causes the initially almost inactive amorphous alloy to become a stable active catalyst. The activity of the resulting catalyst exceeds the activity of polycrystalline iron by more than an order of magnitude (*2*). The transformation occurs well below the bulk glass transition temperature and depends on the presence of hydrogen in the surrounding atmosphere. Another type of activation can be achieved by exposing the catalyst at 700 K to a short pulse of oxygen. This treatment causes the activity to rise within minutes to similar values as they are obtained after several weeks of self-activation during the catalytic run.

The transformation results in a glass to crystalline transition and the formation of two types of iron. The vast majority is α iron, and a small amount of iron with a larger lattice constant is attributed to metastable δ iron. Zirconium does not form crystalline alloys under these special conditions of activation, but becomes oxidized to poorly ordered zirconia. Photoelectron spectroscopy indicated (*1*) that a large fraction of the surface consists of elemental iron covered with a thin oxide layer which is considered to be a transfer artifact.

The present part of the communication describes the morphology of the system. First, we investigate the surface morphology of the amorphous precursor alloy using both scanning electron microscopy (SEM) and the novel scanning tunneling micros-

0021-9517/87 $3.00

copy (STM) (*3*). Subsequently, we show how the activation dramatically alters the surface morphology. A flowchart of the events which shows the evolution of essential features with time will be presented in the conclusion of this part.

EXPERIMENTAL

Samples of the $Fe_{91}Zr_9$ catalyst from various batches and after different catalytic testing were investigated as chips as they were filled in the reactors (see the Experimental section in (*1*)). Individual chips were mounted on small pieces of graphite and without any surface coating introduced via the side entry stage into a JEOL CX 200 TEMSCAN microscope. Investigations were carried out at 200 kV with the minimum beam size and beam current obtainable. Photographic recording was done on a 9 × 7-in. film with exposures of 100 and 1000 sec for the high-resolution images. Elemental microanalyses were performed with a Link 270 EDX system. The detector could be operated either with or without a Be window. For analysis of light elements smaller beam voltages of 100 kV often proved to be beneficial. Analyses were always recorded with several orientations of the specimen in order to estimate the absorption influence on the results which is particularly important for the light elements at energies below the zirconium L line. For this reason no quantitative elemental analysis by EDX was attempted.

For the STM experiments a freshly prepared sample of the alloy was introduced as 1 cm^2 of foil. After baking at 450 K good quality images were obtained. The instrument is homemade and works in a UHV chamber of 10^{-10} Torr base pressure. Good quality high-resolution images were also obtained from these surfaces; we report here only on the low-resolution results. In the light of the severe structural transformations associated with activation we regard the surface details of the precursor alloy observed at high resolution as not typical of the active catalyst. The imaging conditions were 2 V polarization voltage across a W tip and 1 nA tunneling current. The polarization voltage could be reduced for high-resolution imaging down to 20 mV, indicating only a very thin oxide overlayer (see also UPS data in (*1*)). The images were digitally recorded and are shown both in the as measured state and in a special computer processed form. The processing involved first transformation in the top side view and then construction of a height contour map.

RESULTS

1. The Precursor Alloy

The amorphous metal precursor was produced by the melt spinning technique. This involves the spraying of a rectangular profiled jet of liquid metal on a rapidly rotating polished copper wheel. The process was carried out in high vacuum. The resulting ribbon exhibits on the vacuum side a shiny finish and is more dull on the wheel side. After grinding the chips show a roof tile pattern which originates from the zentrifugal milling tool.

The as cast ribbon exhibit very little structure in the optical microscope and the same holds for SEM images. In Fig. 1, a typical medium resolution SEM image is displayed. It shows a casting defect which is used as a landmark. The horizontal line pattern and the gray contrast arise from the insulating surface oxide layer. This layer is invisible on the shiny side of a fresh sample and forms within several months to the state displayed in Fig. 1A. We state the inhomogeneous thickness of this layer seen in the dark spots and contours of the casting defect. This light–dark contrast arises as a conductivity contrast which was verified by observation of the absorbed current images of similar surfaces. It is a typical feature of the amorphous state of many alloy systems.

Closer inspection of the image from the vacuum side of the ribbon reveals a system of tiny grooves which is redrawn in Fig. 1B. The direction of the grooves is exactly

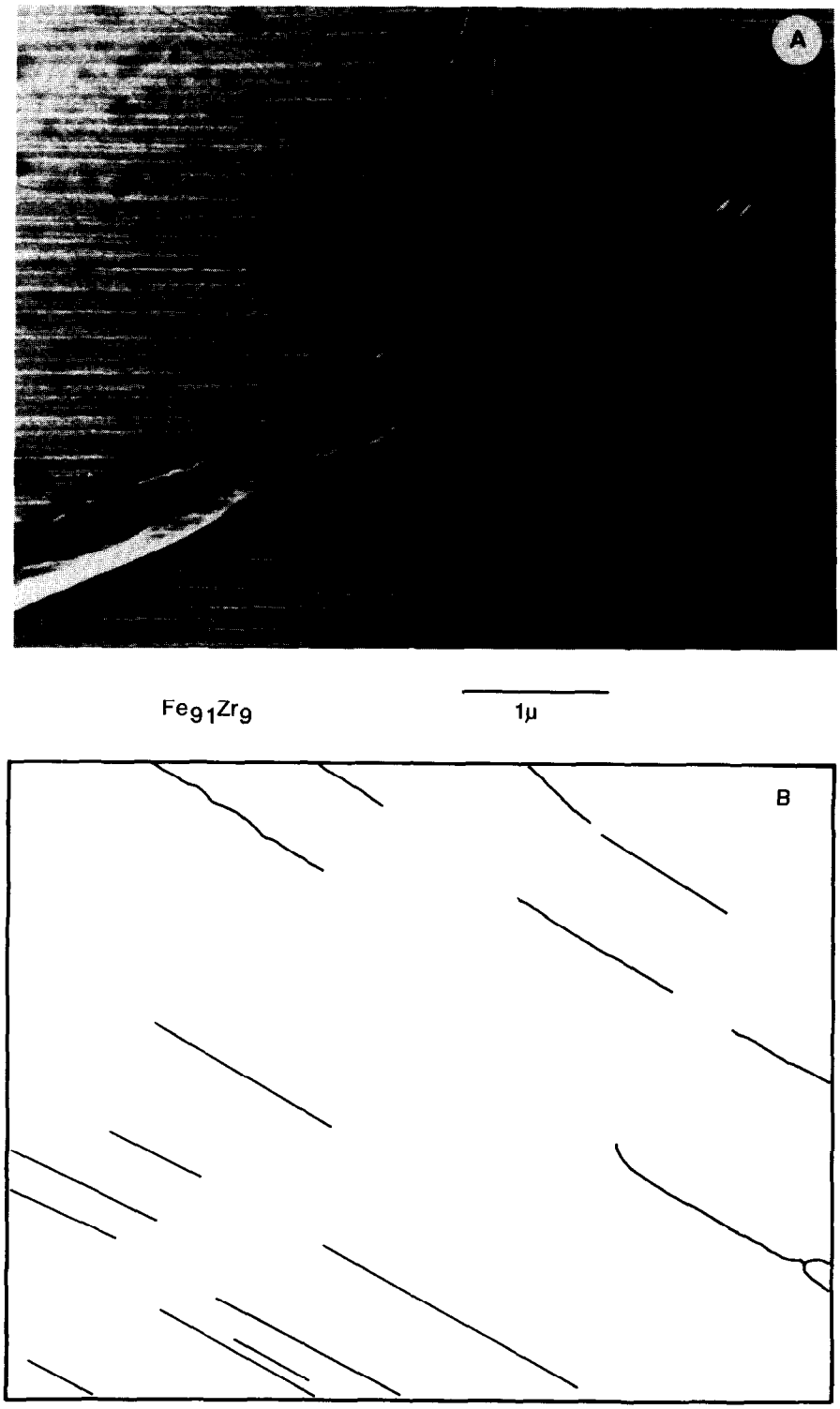

FIG. 1. Surface morphology of the shiny side of freshly prepared $Fe_{91}Zr_9$. In the SEM image of (A), a system of fine grooves which is sketched in (B) has been found. This and all the following SEM images were taken at 200 kV beam voltage without any sample coating.

parallel to the ribbon edge. These grooves are believed to arise from inhomogeneous cooling of individual microdroplets of the liquid alloy. Too rapid cooling of the edges of these droplets prevent them from forming a homogeneous solid without "grain" (droplet) boundaries. This observation is important for the discussion of the reactivity of such a surface which is in fact not as homogeneous and featureless as might be deduced from optical inspection. A similar observation and interpretation of the microstructure of amorphous copper zirconium has recently been reported (*4*).

The detection of signs of microheterogeneity prompted us to study the catalyst precursor surface with STM too. A more detailed knowledge of the prefabricated micromorphology would be valuable for the discussion of the structure of the active catalyst surface. Figure 2 summarizes the results. We show three STM images in both the as measured form and after replacing the skew perspective by a top view using computer processing. In STM the observer sits very close to the surface and has nearly a side view on the surface; i.e., the surface profile in the direction of the surface normal is strongly overemphasized. This depth resolution which is a unique advantage of STM is nearly absent in high-resolution SEM, where the observer sits on the surface normal far above the area of observation. Therefore the computer processed images generate the same perspective as obtained from SEM with additional depth information contained in the gray scale of the contour plots. The areas displayed in Fig. 2 represent a section of ca. 2×2 mm of the area imaged in Fig. 1.

The STM images in Figs. 2A and 2B reveal a rich microstructure which consists of smooth hills several hundred angstroms in diameter and less than a hundred angstroms in height. We state again a strong orientation similar to the groove system seen in Fig. 1. The degree of orientation is, however, strongly overemphasized by the STM perspective as follows from comparison of the direct images with the processed images. In these images we see clearly how the surface is composed of small flat islands separated by narrow and in part steep U-shaped valleys.

The inset in Fig. 2B shows how a boundary between two islands which is parallel to the scan direction can get lost at insufficient resolution, an indication for the narrow and steep profile of the valley. These valleys are believed to be the fine structures of the coarse groove system seen in Fig. 1. They also arise from inhomogeneous cooling of microdroplets. These four images show that the surface of the precursor alloy is not flat, but consists of flat droplets several hundred angstroms in size with clear valleys separating them.

Less frequently the islands are not smooth but show a pronounced structure as seen in Fig. 2C and, in particular, at the bottom of the processed image. Note again how the roughness of this surface is underestimated by the flat perspective of the original STM image. Such structures may arise from instabilities of the jet of liquid microdroplets. Note also the pronounced anisotropy of all structures. The special axis seems to be the growth direction of the ribbon.

At tenfold higher enlargement it becomes apparent that there is no regular pattern on the atomic scale which is expected from the amorphous nature. There was also no sign of cluster structures sticking out from the surface. It could be clearly recognized, however, that there is a finer organization of the smooth surfaces of the droplets. This structure is almost visible in the scans from Figs. 2A and 2B and consists of an irregular corrugation of the surfaces with an average distance of the maxima of several tens of angstroms and an amplitude of below 10 Å. This structure may represent frozen waves excited on the surface of the formerly liquid microdroplets and preserved by the rapid quenching rate of ca. 10^6 deg/sec.

All the rich microstructure of the, at first glance, flat and homogeneous alloy seems

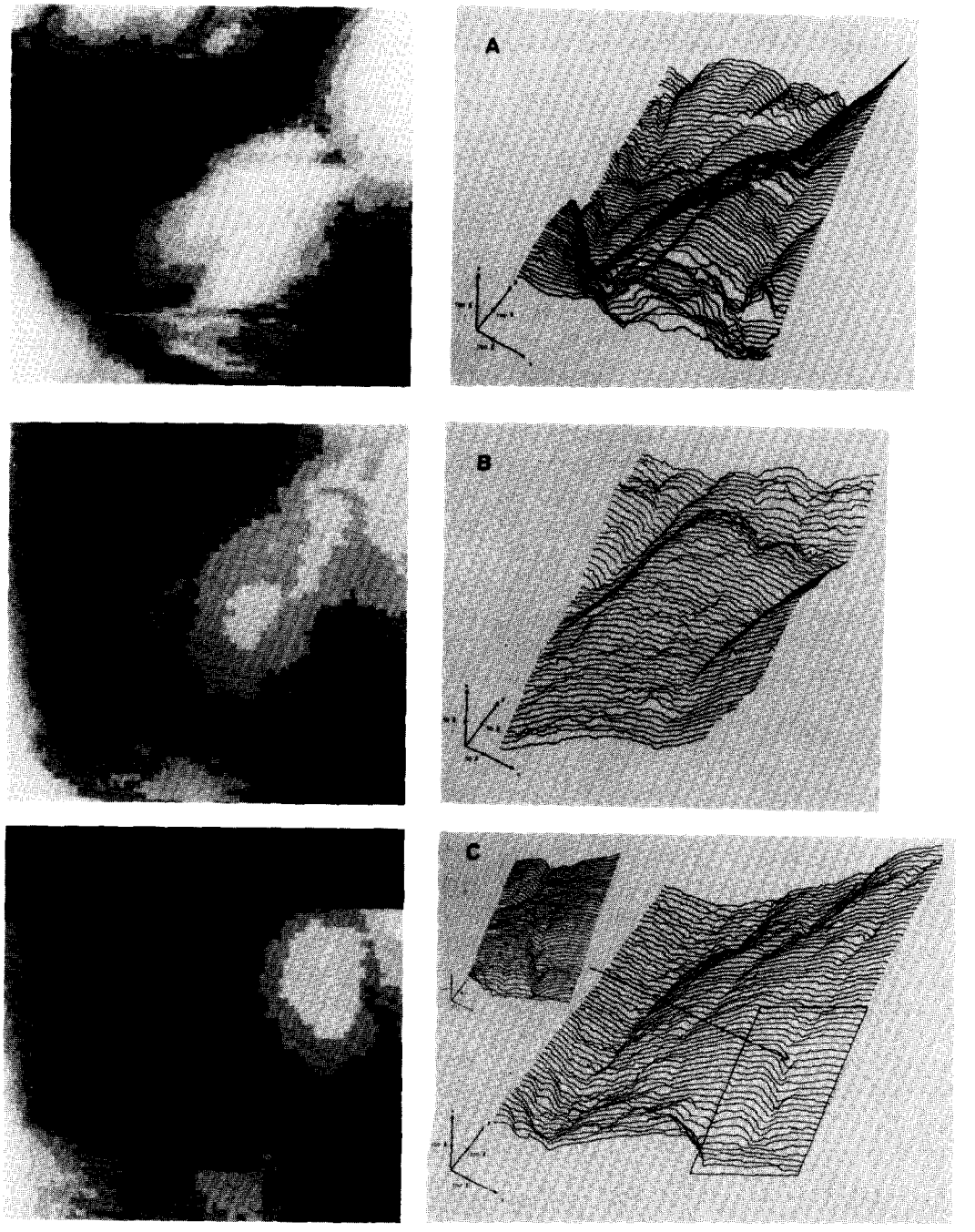

FIG. 2. Typical low-resolution STM images of the shiny side of freshly prepared amorphous $Fe_{91}Zr_9$. The scale in the three main figures is 100 Å/unit, and 50 Å/unit in the inset of (C). The computer-processed images always represent a slightly smaller area than the direct recordings. The height difference between successive gray tones is 5 Å.

to arise from the special solidification process of the amorphous alloys. This structure provides a key to the answer of the question of why amorphous alloys are potentially valuable precursors for catalysts if they are no longer amorphous during reac-

tion. The fabrication process of rapidly quenching provides a microstructure of disk-shaped metal particles which is an uncommon morphology in heterogeneous catalysis.

2. *Activation of the Precursor*

Next we will describe the changes that occur in the surface morphology during activation as they are detected with SEM. For this purpose two series of samples activated during reaction and activated with an oxygen pulse were investigated. The samples of each series were taken from catalysis runs interrupted after various times on stream. The conditions of the catalytic tests were stoichiometric gas feed at 9 bar pressure, 700 K reaction temperature, and activation times between 24 and 1500 h. In the following, the results will be presented in such a way that common and different aspects of the typical surface structures become apparent. The images thus do not represent the historic development of the morphology. The correct sequence of events in time will be discussed in the conclusions.

In Fig. 3 the different coarse morphologies of slow and of oxygen activated samples after ca. 200 h on stream are shown. In Fig. 3A we see anisotropic segregation of worm-like objects which prove to be stacks of thin disks with their short axis oriented parallel to the surface (Fig. 3B). The remainder of the formerly smooth surface is now covered with a dense agglomerate of an insulating material (light areas in Fig. 3A). The individual disks are thin enough to be transparent for the 200-keV electron beam (the nebulous contours in Fig. 3B represent a single disk attached askew to the stack seen in the center of the image).

Oxygen activation results in a dense coverage of the initial surface with large spherical particles without any discernible substructure (Fig. 3C and 3D). The free areas between the spherical particles are covered with the same insulating agglomerate as seen on the slowly activated samples.

EDX identified the disks as consisting of pure elemental iron, while the spherical particles consist of iron oxide admixed with some zirconium and silicon. The insulating agglomerate is made up of zirconium compounds, presumably of oxides and nitrides. From comparison with XPS results (see part 1 (*1*)) we conclude that the nitrides must form a bulk phase covered only with a oxide layer thick enough to hide most of the nitrogen from detection by XPS.

Crystallization and the observed segregation phenomena should result in a volume change of the bulk material. One expects to see cracks in the surface. A network of cracks is indeed observed with some characteristics displayed in Fig. 4. In contrast to cracks in crystalline materials, where they often follow line defects and grain boundaries with special orientations, the cracks in the amorphous solid exhibit no long-range correlation. They rather seem to depict the microstructure of spherical droplets, as may be deduced from the contours of Figs. 4A and 4B. Closer examination shows that the cracks produce some kind of wall structure (Fig. 4B). This wall structure is not detectable after long activation periods. We conclude that Fig. 4B represents a "snapshot" of partially transformed microdroplets with a still amorphous central region. The transformation would then start at the edges of the microdroplets and proceed in a uniform reaction front to the center of the droplet.

The material of the wall structure is the same as that of the insulating agglomerate. It is displayed in high resolution in Fig. 4C. Such a morphology may well account for the increase in total BET surface area observed (*1*).

After 450 h of activation a surface morphology as displayed in the survey image of Fig. 5A is the common structure. We see a marked heterogeniety with three major elements. At the left of the photo a meander-like network structure can be seen. This is

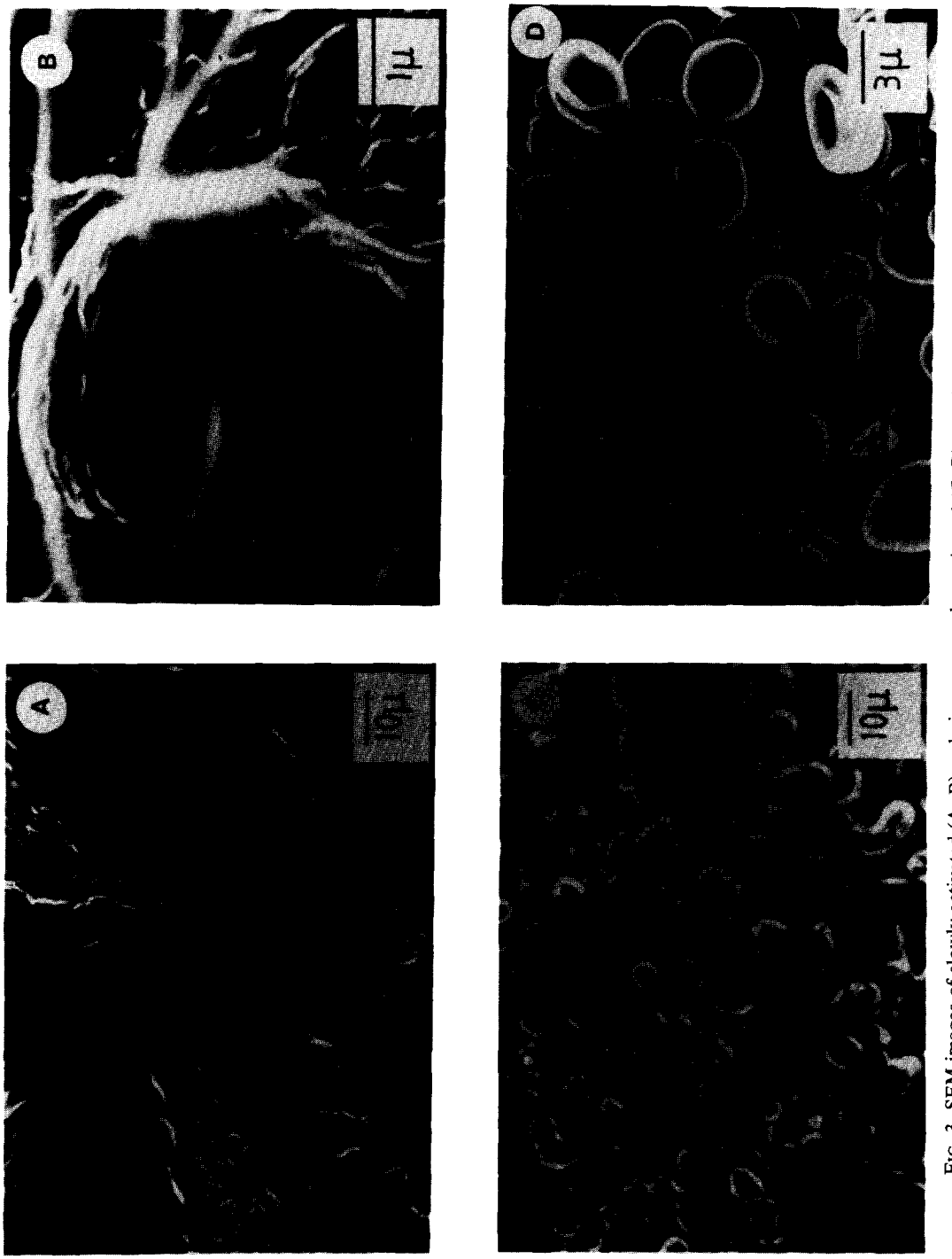

FIG. 3. SEM images of slowly activated (A, B) and via-oxygen-pulse-activated (C, D) samples, both after ca. 200 h on stream.

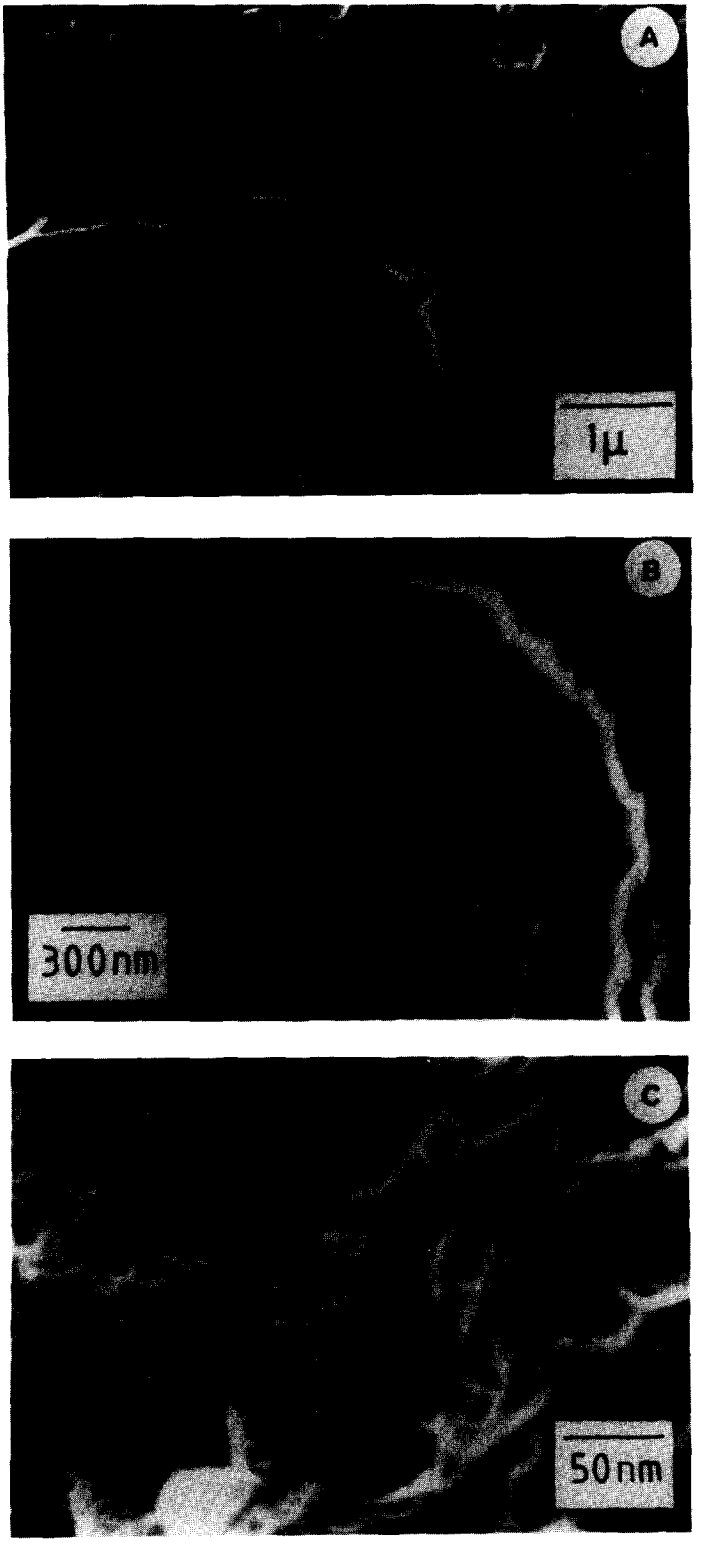

FIG. 4. SEM images of the cracks formed during activation. The cracks stay visible for all times after 24 h activation. After long activation the core and shell structure visible in (B) has disappeared.

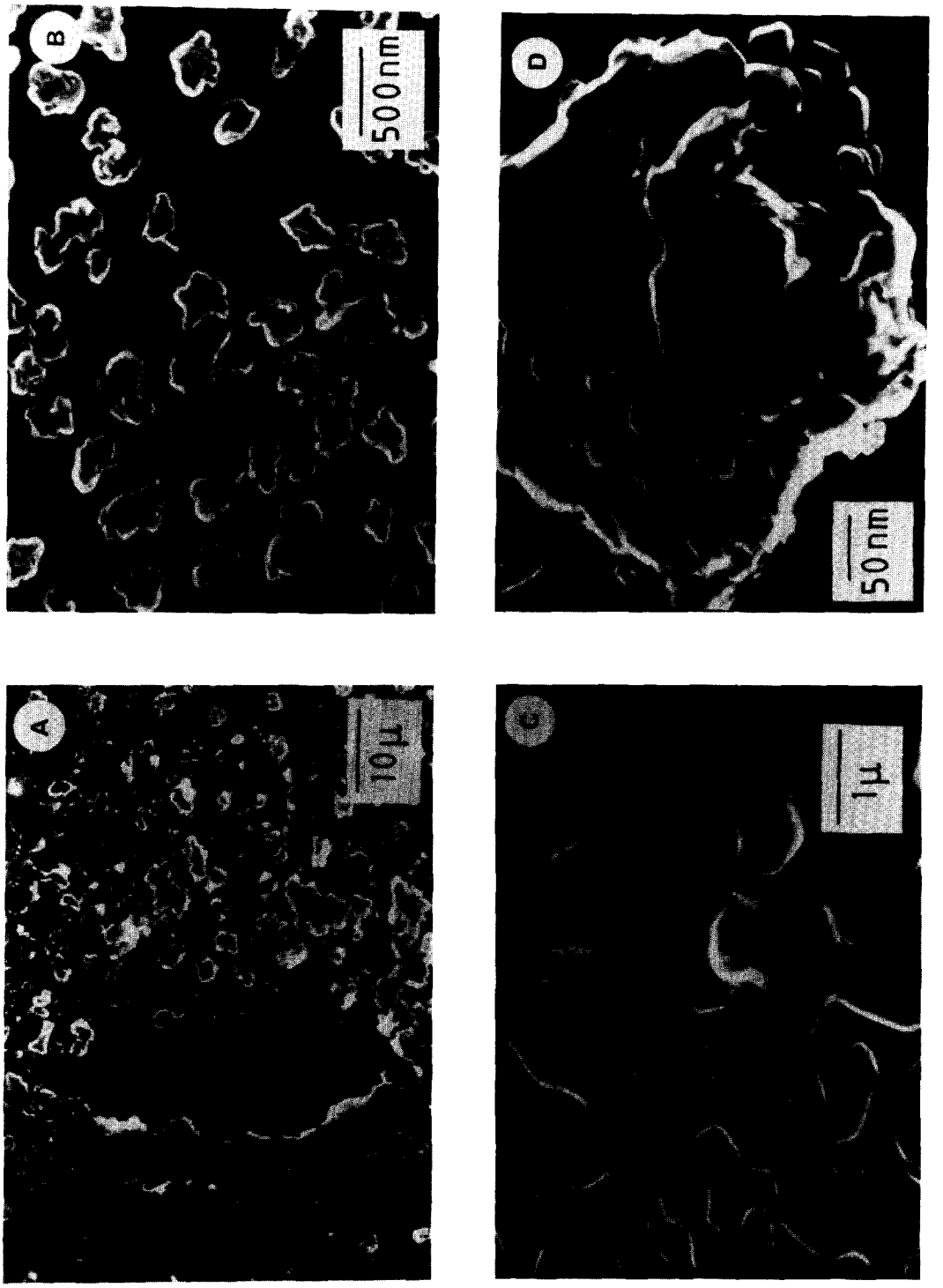

FIG. 5. SEM images of slowly activated samples after ca. 450 h corresponding to almost complete activation. The particles in (B) and (D) are nonconducting.

enlarged in Fig. 5C. More to the center we see a reaction front along a crack (light line) followed by a rather featureless area (presumably not yet transformed). The right hand part consists of small irregular particles (enlarged in Fig. 5D) supported on the same meander structure as in the left hand side of the image. We want to point out that this meander structure also develops under the spherical particles of the samples activated by an oxygen pulse. This structure is the most common and prevailing feature of all activated samples.

The meander structure and the irregular-shaped particles of Figs. 5C and 5D, respectively, represent two very different materials as emerged from the EDX measurements. The irregular particles consist of a mixture of zirconium oxide and nitride with traces of some contaminants (Si, K, Cl, Ca) originating from the glass and inert filling material of the reactor. The meander structure on the other hand is formed from predominantly iron metal.

3. *The Microstructure of the Types of Iron*

The important structural details found during activation are two types of iron, one forming stacks of disks and the other forming a meander network. At least one of them is considered to be the catalytically active species. An attempt is made therefore to further describe the micromorphology of these two forms of iron which are both uncommon to conventional ammonia synthesis catalysts.

In Fig. 6 the less common type of stacks of iron is shown in greater detail. The stack is oriented perpendicular to the surface, and the individual members seem to reproduce the system of grooves seen in the surface of the amorphous alloy (see Fig. 6A, note the sectioning of a package of disks). The individual disks are far larger than the microdroplets found in the precursor alloy. High-resolution images such as in Figs. 6B and 6C of individual disks show that they are composed in both thickness (Fig. 6B) and lateral extension (Fig. 6C) of smaller units. These may well be the microdroplets of the precursor organized before activation in stacks with the small axis of the disks oriented perpendicular to the surface (see Fig. 2).

Details of the meander structure are displayed in Fig. 7. The top surface of this structure is usually flat except for occasional iron particles and whiskers of α iron as shown in Fig. 7A. Both whiskers and pyramidal particles were observed more frequently on oxygen-activated samples than on slowly activated samples.

The meander structure originates from a layer of irregular-shaped iron particles with a uniform thickness much smaller than its lateral dimensions. As Figs. 7B and 7C demonstrate, these particles show well-developed edges with step structures of a few unit cells in height (Fig. 7C). Sometimes small crystals can be found in the voids between the large crystals. The well-developed shape of these crystals is an indication that the material crystallized slowly. Therefore this structure develops not at the beginning of the transformation when the stacks of disks prevail, but at the end of activation when most of the total surface is covered by these large iron crystals and only few stack structures are found.

The smaller crystals seen in Figs. 7B and 7C are much more prominent in oxygen-pulse-activated samples. This also indicates that the growth of the crystals is a slow process which may determine the rate of final activation.

Figure 8 shows the surface texture of the two types of iron at the highest possible resolution with SEM. The top image is from the disks, whereas the bottom image was taken from the top surface of a large crystal from the meander structure. The different resolution power is partly due to geometrical constraints and partly due to the different specimen thickness. From Fig. 8 (top plate) we find confirmation that individual disks are composites of thinner units (com-

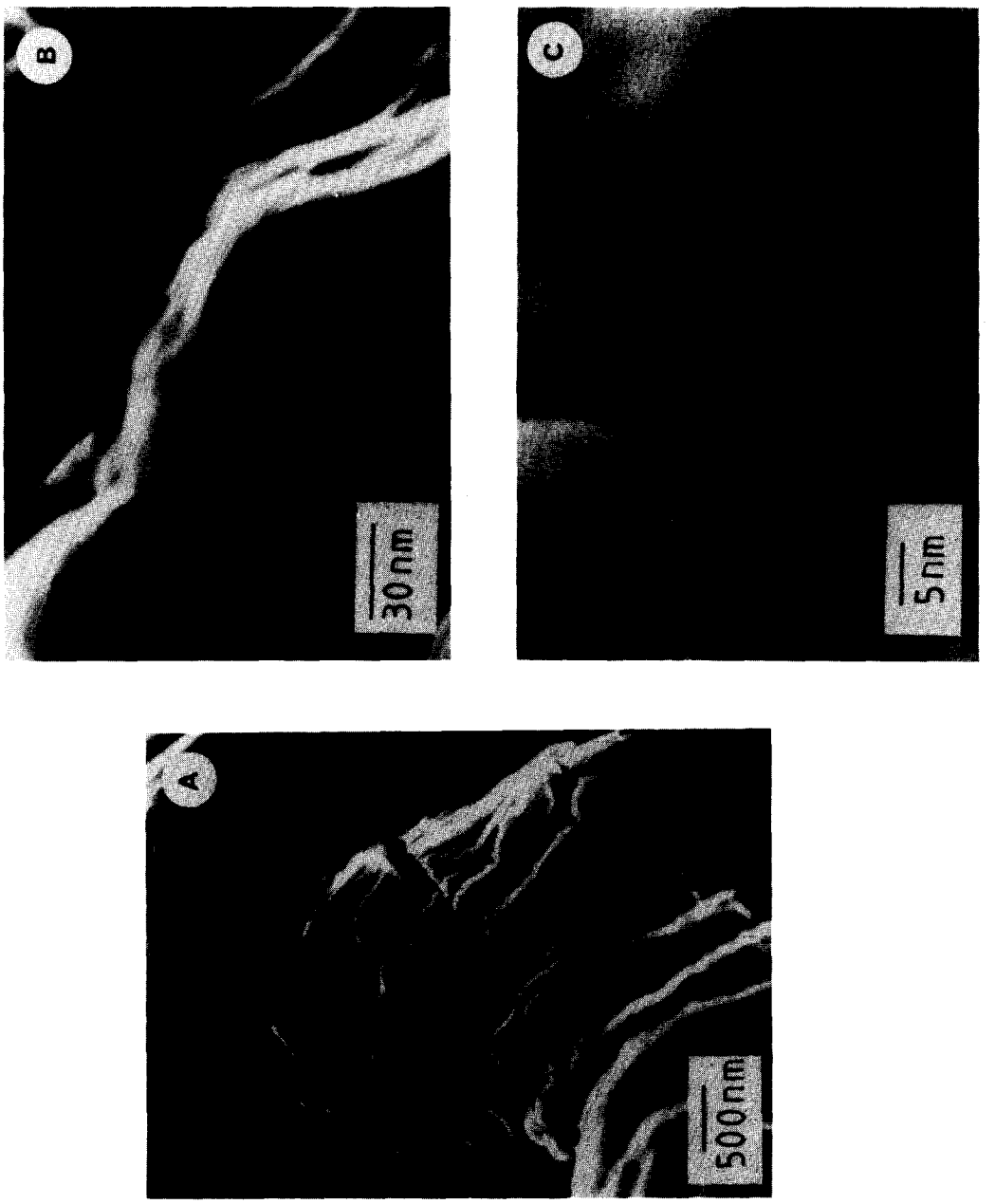

FIG. 6. High-resolution SEM images of the stacked disk feature from a slowly activated sample (400 h on stream). Note the mesopore formed by the contact of 4 microunits in (C).

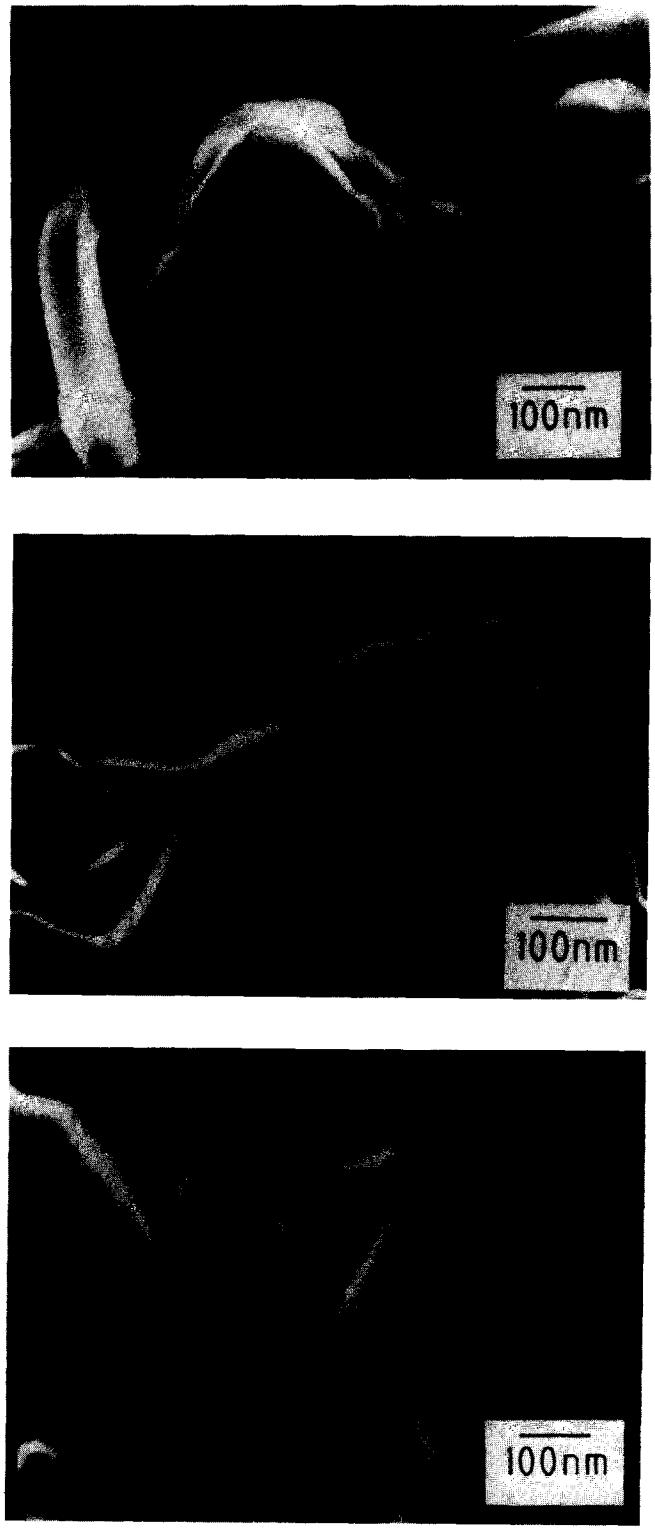

FIG. 7. SEM images of the meander structure of a slowly activated sample (220 h on stream). The pyramidal particles and the whiskers (top plate) are more common with oxygen-pulse-activated samples. Note the resolution of fine step structures at several locations in the bottom plate.

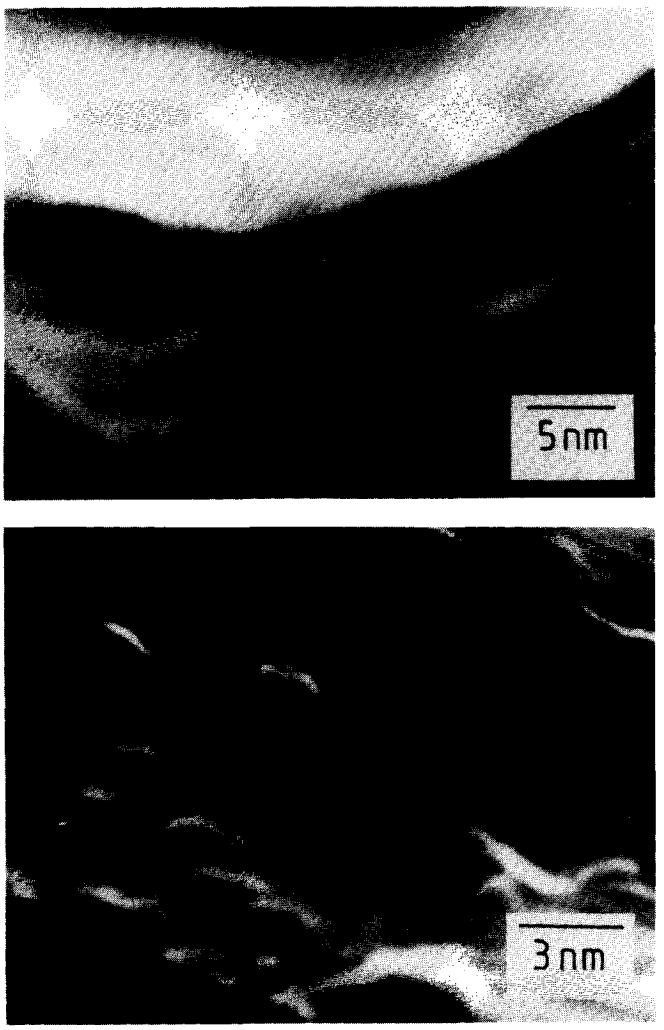

FIG. 8. Surface texture of the two types of iron at maximum resolution. (Top) Surface of a microunit (see also Fig. 6C) from the stacked disk feature; (bottom) top surface of a large crystal from the meander structure.

pare with Fig. 6C). The uniform contrast from the top surface does not mean that this surface is featureless, its structure could not be resolved due to methodical limitations.

From Fig. 8 (bottom plate), we learn that the surface of the regular-shaped crystals is in fact not smooth but seems to consist of an array of nearly equally sized clusters of iron. The resolution does not permit one to decide whether the space between the clusters is filled or remained open to form micropores. We can estimate that a rich distribution of reaction sites is offered from such a surface texture.

DISCUSSION

Metallic glasses are often considered as supercooled liquids which should hence be homogeneous and isotropic. This picture of a nonreactive solid is not consistent with the ease of the solid state reactions involved in the transformation of the catalytically inactive state to the catalytically active state. Investigation of the micro-

structure of the surface of the amorphous metal gave evidence for a pronounced secondary structure involving disk-shaped elements of roughly 100 by 500 Å size which may be composites themselves from nano- or microcrystals. Such an organization of a solid is difficult to detect with diffraction methods but was recently postulated from the interpretation of neutron small-angle diffraction data in similar iron alloys (*5*). The source of this secondary structure is the preparation process of rapidly quenching by melt spinning. Nonuniform cooling rates and the formation of microdroplets in the casting process cause a microstructure with irregular boundaries between the individual elements.

The disk-shaped elements in the precursor structure influence the formation of the final catalytically active particles. This was seen either directly (stacks of disks) or may be concluded indirectly (the locally liberated heat of crystallization supplies energy locally to solid state reactions). Disk-shaped iron particles as well as the well-developed faces of the larger iron crystals are uncommon morphologies in conventional ammonia synthesis catalysts. They are considered as a direct consequence of the special nature of the precursor alloy. The effect of the metallic glass on the catalytic activity is thus not to influence the electronic structure of the catalyst, but as it was concluded from photoemission results (part 3 (*6*)), to geometrically influence the catalytic activity by forcing the active iron to crystallize in a special morphology which is not obtained upon reduction of iron oxides (the conventional activation process for ammonia synthesis catalysts).

On the basis of the present results, it cannot be decided which structure carries the catalytic activity. Fully activated samples predominantly exhibit the large

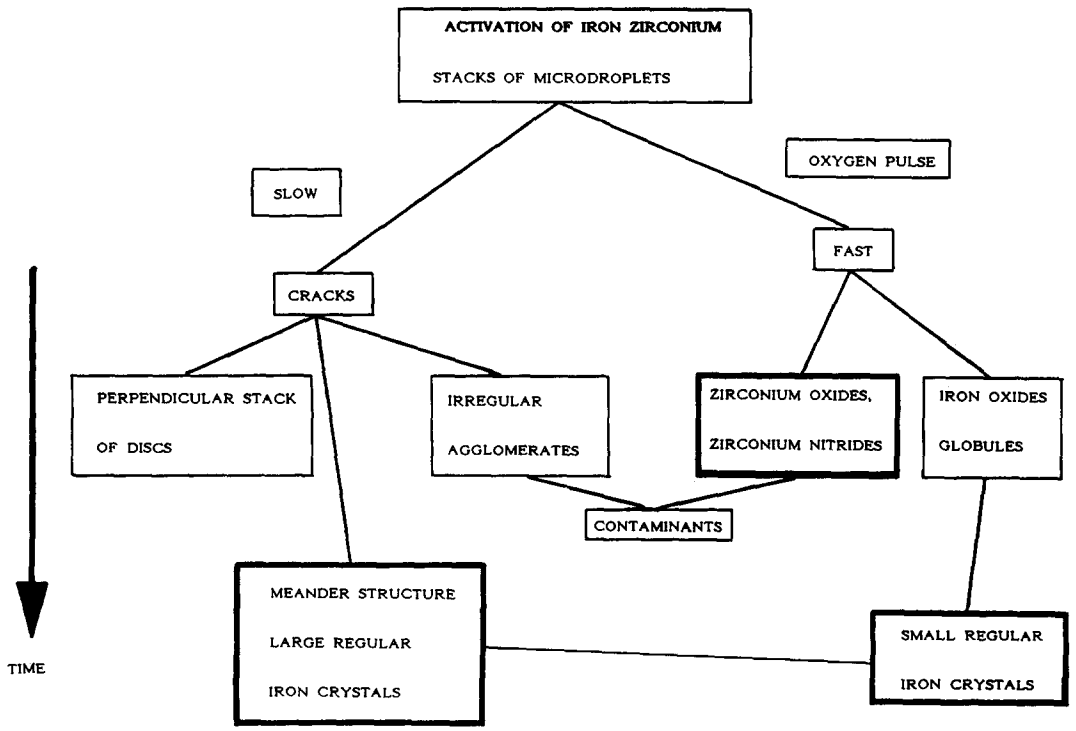

FIG. 9. Schematic representation of the connection and history of evolution of the various features found in the study of the activation process of $Fe_{91}Zr_9$ catalysts. The heavy framed species are the predominant features after full activation of the catalysts.

crystals of the meander structure, but the stacked disk feature can also be detected. Comparison of the morphological analysis with the XRD results and the history of formation imply the assignment of δ iron to the stacked disk feature and α iron to the meander structure. This assignment remains speculative, however, since the volume-to-surface sensitivity ratio of XRD and SEM is vastly different.

The SEM investigation of the activation process revealed that a variety of different particles are present. From the results described in (*1, 6*), we conclude that it is elemental iron which is catalytically active. The other species of particles are considered to be only spectator species.

In Fig. 9 we summarize all observations and show their historical order. We distinguish two types of activation by the time required to reach steady-state conversion to ammonia. Both processes lead via different pathways to similar final surface morphologies. They consist of regular-shaped iron crystals in large and small sizes, of agglomerates of oxides based on zirconium oxide, and of a minority phase of iron metal (not highlighted in Fig. 9). The microscopic studies support the conclusion from our spectroscopic investigations (*1, 6*) that the catalyst is metallic iron in an unusual geometric form.

ACKNOWLEDGMENTS

All samples were prepared by P. Reimann, and the manuscript was carefully read by G. Loose. We acknowledge the generous access to the electron microscopy facilities at the department of Physical Chemistry of Cambridge University given to us by J. M. Thomas and D. A. Jefferson. One of us (R.S.) is grateful for financial support to the Swiss National Science Foundation during his stay at Basel. The whole project was financially supported by Lonza AG, Switzerland.

REFERENCES

1. Baiker, A., Schlögl, R., Armbruster, E., and Güntherodt, H. J., *J. Catal.* **107,** 221 (1987).
2. Armbruster, E., Baiker, A., Baris, H., Güntherodt, H. J., and Schlögl, R., *J. Chem. Soc. Chem. Commun.*, 299 (1986).
3. Binnig, G., and Rohrer, H., Helv. *Phys. Acta* **56,** 481 (1983).
4. Blank, M., Caesar, Ch., and Köster, U., *in* "Rapidly Quenched Metals" (S. Steep, and H. Warlimont, Eds.), p. 883, 1985.
5. Boucher, B., Chieux, P., Covert, P., and Tournarie, M., *J. Non-Cryst. Solids,* **61–62,** 511 (1984).
6. Baiker, A., Baris, H., and Schlögl, R., *J. Catal.* **108,** 467 (1987).